Applied Surface Science 691 (2025) 162663

Contents lists available at ScienceDirect

Applied Surface Science

journal homepage: www.elsevier.com/locate/apsusc

Full Length Article

Carrier transport behavior and piezoresistive mechanism of Cr-DLC nanocomposite films

Wenlong Zhang [a,b], Peng Guo [b,*], Yulong Yang [b], Hao Li [b], Wei Yang [b], Rende Chen [b], Bo Xie [a], Aiying Wang [b,c,*]

[a] College of Chemical Engineering, Zhejiang University of Technology, Hangzhou 310014, China
[b] State Key Laboratory of Advanced Marine Materials, Ningbo Institute of Materials Technology and Engineering, Chinese Academy of Sciences, Ningbo 315201, China
[c] Center of Materials Science and Optoelectronics Engineering, University of Chinese Academy of Sciences, Beijing 100049, China

ARTICLE INFO

Keywords:
Diamond-like carbon film
Carrier transport mechanism
Energy band structure
Piezoresistive behavior

ABSTRACT

Compared with silicon and polysilicon piezoresistive materials in MEMS, diamond-like carbon (DLC) films are promising candidates for applications in harsh corrosive environment. However, the underlying mechanism between piezoresistive properties and carrier behavior is still lacking study yet due to the complexity in atomic bonds. To develop new carbon-based sensors for harsh environments, we synthesized the Cr-containing DLC films with Cr content changed from 0.64 to 23.17 at.%. The results showed that increasing Cr content enhanced the conductive phases distributed in the amorphous sp^3 matrix. Nevertheless, a small amount of Cr_3C_2 nanocrystals formed when Cr content reached 11.05 at.%. All Cr-DLC films exhibited the semiconductor behavior in the range of 150–350 K. However, the threshold voltage of I-V plot disappeared once the Cr content exceeded 11.05 at.%. Similarly, the optical bandgap decreased from 3.55 to 2.49 eV as Cr content increased from 0.64 to 23.17 at.%. The Fermi level was closer to the valence band edge, indicating p-type semiconductor characteristic. For the sample with an appropriate Cr content of 1.38 at.%, it had the highest gauge factor of 22.8. Its minimum valence band offset of 0.89 eV resulted in a significant change in the tunneling process under applied strain, which explains its notable piezoresistive effect.

1. Introduction

Silicon and polysilicon are widely preferred and used as piezoresistive materials in microelectromechanical systems (MEMS) technologies [1,2], with stable gauge factor (GF) range from 8.6 to 175 [3,4]. However, with the rapid development of Hi-Tech, traditional silicon-based sensors cannot operate well in harsh environments due to their poor mechanical properties, low bandgap [5], increased p-n junction leakage current [6]. Given potential for mechanical damage, corrosive media, high radiation and high temperatures in such environments, it is both important and challenging to develop new sensitive materials and sensing technology with high stability.

Diamond-like carbon (DLC) films, which are widely used as protective and electronic materials, are mainly composed of C-sp^3 (diamond) and C-sp^2 (graphite) structures [7,8]. In consideration of their outstanding high-temperature resistance up to 680 °C [9], excellent chemical stability [10,11], significant piezoresistive effects [12–15] with GF up to 1000 ~ 3200 [16], and high compatibility with the existing MEMS [14,17], DLC films are promising candidates for reliable sensing in harsh environments.

In practical applications, various metal-containing DLC films, such as Cr [18], Nb [19], W [20] and Ni [16], Cu [21,22] atoms, have garnered significant attention due to their potential to achieve both high GF and low temperature coefficient of resistance (TCR). Intrinsic DLC films are amorphous semiconductors and typical exhibit high TCR values up to 8000 ppm/K [23]. For example, Koppert et al. [24] found that a DLC film with a Ni content of 52 at.% showed a GF of 14 and near-zero TCR within the temperature range of 90–400 K. Similarly, Yan et al. [22] pointed out that with the increment of Cu content, the GF of DLC decreased rapidly from 5.6 to 1.4, while TCR values changed from −4980 to + 294 ppm/K. The doping of the metals resulted in an overall decreasing trend in the TCR, but the GF did not show a clear regularity with metal doping. Additionally, significant progress has also been made in understanding the piezoresistive mechanism of metal-containing DLC

* Corresponding authors at: State Key Laboratory of Advanced Marine Materials, Ningbo Institute of Materials Technology and Engineering, Chinese Academy of Sciences, Ningbo 315201, China.
E-mail addresses: guopeng@nimte.ac.cn (P. Guo), aywang@nimte.ac.cn (A. Wang).

https://doi.org/10.1016/j.apsusc.2025.162663
Received 27 November 2024; Received in revised form 5 February 2025; Accepted 9 February 2025
Available online 10 February 2025

films. Typically, Meškinis et al. [21] proposed percolation-tunneling model, while Tibrewala et al. [13] proposed a thick film resistors (TFR) model and suggested that applied strain can alter the carrier transport paths. Yan et al. [22] confirmed both thermal activation transport and three-dimensional Mott-type variable range hopping (VRH) conduction in different temperature ranges, and explained the electrical properties and piezoresistive effects of Cu-DLC through carrier tunnelling processes between conducting phases in an insulating sp^3 matrix.

While the existing theories provide general descriptions of the carrier transport behavior and piezoresistive process in metal-containing DLC films, they neglect at least three factors. First, the different bond characteristics between various metal and carbon atoms can significantly alter the bond structure and electronic states of the metal-containing DLC films [25,26]. Second, the incorporated metal atoms can either dissolve or aggregate into nanoscale metal/carbide particles in DLC matrix, depending on their content, leading to diverse microstructures and carrier behaviors [27]. Finally, as amorphous semiconductors, DLC films are distinguished from crystalline semiconductors by the presence of localized state conductance in addition to extended state conductance. However, the role of bandgap on their carrier transport behavior and piezoresistive mechanism is often neglected and rarely discussed [28]. Therefore, the design of high-performance DLC sensitive materials is complex and lacks theoretical guidance.

In our previous study, Cr-DLC films exhibited lower residual stress of 0.46 GPa [29–31], excellent corrosion resistance [32] and superior wear resistance [33]. Additionally, Cr have been found to catalyze the formation of sp^2-C bonds in DLC [34] and reduce the TCR [18]. Thus, in this study, a series of Cr-DLC films were prepared using high power impulse magnetron sputtering (HiPIMS) technique, since HiPIMS is better in producing dense DLC films suitable for some corrosive environments. The effects of Cr content on the structure, composition, electrical properties, and energy band structure of Cr-DLC films were investigated. Furthermore, we conducted an in-depth discussion on the carrier transport mechanism and piezoresistive mechanism.

2. Experimental details

2.1. Sample preparation

Fig. 1 presents a schematic diagram of the HiPIMS system. A rectangular target, spliced with one chromium target (20 × 100 × 7 mm, 99.95 % purity) and one graphite target (380 × 100 × 7 mm, 99.99 % purity) was employed. To characterize microstructure, energy band structure, electrical properties, and piezoresistive behavior of the Cr-DLC films, various substrates were employed: n-type silicon (100), n-type silicon (100) substrates coated with a 300 nm-thick SiO_2 film through dry oxidation, high-conductivity silicon, and Al_2O_3 (0001) wafers. Before deposition, all the substrates were cleaned with anhydrous ethanol and fixed on the substrate holder positioned inside the vacuum chamber.

Here, the chromium content was adjusted by varying the distance of the substrates from the chromium target on the substrate holder. The substrate holder was facing and 3.5 cm higher than the sputtering target, and the horizontal distance from the target to the substrate holder was about 11.5 cm. The small piece of Cr target was 10 cm in length and 2 cm in width, had a distance of 2 cm away from the top of the rectangular target. And the samples were named S1, S2, S3, S4, and S5, with a distance of 35, 28, 21, 14, and 7 cm from the top of the substrate holder in that order, respectively. Since the sputtering rate of the chromium target was higher than that of the graphite target, the Cr-DLC sample positioned closer to the chromium target had a higher deposition rate. To exclude the influence of the thickness on their carrier transport and piezoresistive behavior, the deposition times of S1 and S2 were set to 180 min and 140 min, respectively, while the deposition times of S3, S4, and S5 were kept at 120 min, resulting in a similar film thickness of 170 ± 10 nm for all samples.

Once the base pressure of the chamber reached 2.0 × 10^{-5} Torr, all the substrates were cleaned by Ar^+ ions for 20 min with a pulsed bias of −200 V. Subsequently, 100 sccm of Ar precursor gas was introduced to ignite the spliced target for the deposition of the Cr-DLC films. The deposition process was carried out using HiPIMS power of 500 W and a working pressure of 8 × 10^{-3} Torr.

2.2. Characterization method

The cross-sectional morphology and thickness of the Cr-DLC films were observed by scanning electron microscopy (SEM, Verios G4 UC, USA). X-ray photoelectron spectroscopy (XPS, Axis Ultra DLD, Japan) was used to characterize the chemical bonds and elemental content of the Cr-DLC films, with Al (mono) Kα photon energy of 1486.6 eV. The spot size for XPS test was 700 × 300 μ m. Prior to the XPS test, the samples were etched by Ar^+ ion with bias 5 kV for 1 min. Detailed XPS test parameters are available in the Supplementary Information. The

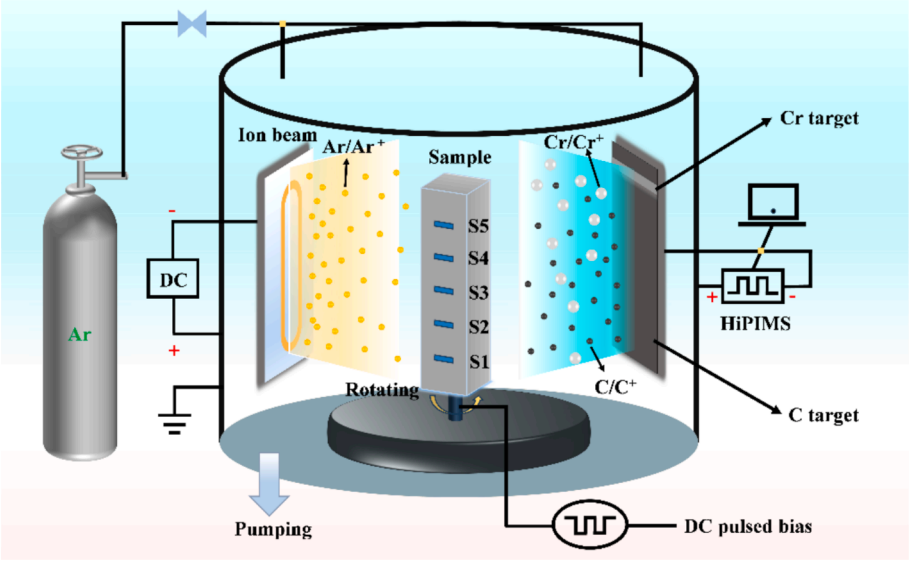

Fig. 1. A schematic diagram of Cr-DLC films deposition system.

carbon atomic bonding structures of the Cr-DLC films were investigated by Raman spectroscopy (Renishaw inVia Reflex, UK, 532 nm). Their microstructure was characterized by transmission electron microscopy (TEM, Tecnai F20, USA), and the sp^2/sp^3 ratio was studied by the electron energy loss spectroscopy (EELS).

To investigate their optical bandgap of the Cr-DLC films, the transmittance spectroscopy was measured within a wavelength range of 200–1600 nm using a UV–visible near-infrared spectrometer (UV/Vis/NIR Spectrometer, Lambda 950, USA). The work function of the Cr-DLC films was determined using ultraviolet photoelectron spectroscopy (UPS, Axis Ultra DLD, Japan). The UPS spectrum was acquired using a He I (21.22 eV) light source. The incident angle was 45°, and the emission angle was 0°. The base pressure was 5×10^{-8} Torr, and bias voltage on the sample was −9.33 V.

The I-V characteristic plots and electrical resistivity of the Cr-DLC films were measured by the physical property measurement system (PPMS, PPMS-EverCool, USA) within a test temperature range of 150 K-350 K. Additionally, their spatial distribution and local electrical properties of the current paths were characterized using a conductive atomic force microscope (C-AFM).

For GF test, the Cr-DLC samples were deposited on silicon oxide substrate with dimensions of 35 × 5 × 0.5 mm. Copper wires were attached at both ends of the test samples using conductive silver paste. The applied strain was exerted using a homemade three-point bending equipment [35,36]. The real-time resistance of the test samples was measured with a desktop multimeter (FLUKE, 8846A), and the corresponding GF was calculated using the following equation [35].

$$GF = \frac{\Delta R}{R_0 \varepsilon} = \frac{l^2}{3t\Delta Y}\frac{\Delta R}{R_0} \quad (1)$$

where R_0 is the initial resistance, ΔR is the change of resistance under applied strain, ε is strain measured by formula $(3\ t{\cdot}\Delta Y)/l^2$. The total thickness of the test sample was recorded as t, and the distance between the two support points on the sample stage was assigned as the effective length l. The deflection was denoted as ΔY.

3. Experimental details

3.1. Microstructure and chemical composition of Cr-DLC films

Fig. 2(a–e) shows the cross-sectional morphology of Cr-DLC films deposited on Si wafers. All samples exhibited similar thickness of approximately 170 ± 10 nm, dense morphology and a clear interface with the Si substrate.

Their XPS spectra and the fitting results were shown in Fig. 3. The content of each element was given in Fig. 3(a), and all Cr-DLC films were composed of C, O, and Cr elements. The presence of a small amount of O atoms might be due to residual oxygen in the chamber during the deposition process [37,38]. The binding energy of the C—Cr bond around 283.2 eV can be set as the binding energy reference in the C1s spectra[39]. The peak position gap between sp^2-C and sp^2-C was set to a content of 0.9 eV in the fitting [40].As the distance of the samples from the top of the substrate holder gradually decreased from 35 cm to 7 cm, the Cr content increased from 0.64 at.% to 23.17 at.%. The C 1 s spectra in Fig. 3(b) revealed the presence of C═O, C—O, C—C (sp^3) hybridizations, C═C (sp^2) hybridizations, and Cr—C hybridizations at around 288.1 eV, 286.1 eV, 284.9 eV, 284.1 eV and 283.2 eV [39], respectively. Notably, the Cr—C peak became more prominent with the highest Cr content. Additionally, as the Cr content increased, the sp^2/sp^3 content also increased from 1.80 to 4.14, indicating that Cr doping was beneficial for the formation of sp^2-C, as shown in Fig. 3(c). XPS comprehensive experimental details, including HiPIMS DLC, all the peak positions, FWHMs, peak shapes, and background subtraction methods for each sample are available in the Supplementary Information.

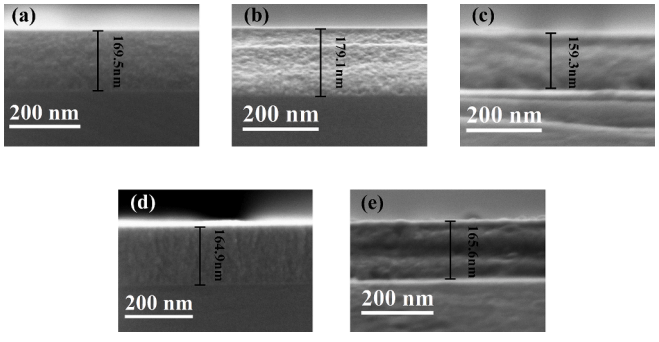

Fig. 2. (a–e) SEM images of the cross-sectional morphology for S1-S5 films with different Cr content.

Fig. 4(a) presents the Raman spectra of Cr-DLC films. All the samples showed two characteristic peaks of amorphous carbon near 1350 cm^{-1} and 1560 cm^{-1}, corresponding to the D and G peaks, respectively. The position of the G peak position (Pos_G), the peak area ratio I_D/I_G and full width at half maximum of the G peak ($FWHM_G$) were determined after Gaussian fitting. In Fig. 4(b), as the Cr content increased from 0.64 at.% to 23.17 at.%, the I_D/I_G ratio increased from 1.30 to 3.16, suggesting that Cr doping can increase the size of sp^2 clusters [41]. It is not directly feasible to quantify information about sp^2/sp^3 from I_D/I_G in Raman tests. Meanwhile, the $FWHM_G$ gradually decreased, indicating that Cr doping increased the disorder of the film structure [42].

Fig. 5. shows the high-resolution TEM (HRTEM) micrographs, selected area electron diffraction (SAED), and electron energy loss spectroscopy (EELS) of Cr-DLC with low (4.27 at.%, S3), medium (11.05 at.%, S4) and high (23.17 at.%, S5) Cr content. In Fig. 5(a), the S3 sample exhibited a homogeneous and dense structure, its corresponding SAED pattern also showed diffuse rings, indicating that the doped Cr atoms were dissolved in the amorphous matrix. When the Cr content reached 11.05 at.% (Fig. 5(b) and (e)), nanocrystals with a diameter of approximately 1.4 nm begin to appear in the HRTEM fringes. The lattice spacing 0.202 nm was obtained from the inverse Fourier transform of their lattice fringes, corresponds to the Cr_3C_2 (240) ($d = 0.199$ nm). With a Cr content of 23.17 at.% in the S5 sample, more Cr_3C_2 nanocrystals with a diameter around 3.3 nm appeared, as shown in Fig. 5(c) and (f). The lattice stripes became more obvious, and the diffraction rings in the SAED pattern can be indexed as the Cr_3C_2 (1 1 1), (240), and (251) planes.

Fig. 5(d) shows the EELS results of the three samples. The EELS curves [43] yield π* peaks near 285 eV and σ* peaks in the range of 290–305 eV, which can be used to compare the characteristics of C═C (sp^2) and C—C (sp^3) hybrid bonds. The intensity ratios of the π* and σ* peaks were found to be 0.11, 0.12, and 0.17 for S3, S4, and S5, respectively. These results indicated that Cr doping can lead to a gradual increase in the sp^2 content, which agreed well with the previous Raman and XPS results.

3.2. Electrical properties

The I-V curves of S1-S5 samples in the temperature interval of 150 K-350 K are displayed in Fig. 6. Overall, the I-V curves of all the samples exhibited favorable linear characteristic and typical ohmic behavior. At a certain temperature, samples with higher Cr content exhibited lower voltages under the same excitation current, indicating their lower resistance. This can be attributed to the increase in conductive Cr and the sp^2 phase.

Fig. 7(a) shows the resistivity versus temperature curves (R-T plots) of Cr-DLC films in the temperature range of 150 K-350 K. For all samples, as the test temperature increased, their corresponding resistivity decreased, exhibiting typical semiconductor characteristic [44]. Moreover, the sensitivity of resistivity to temperature decreased with increasing Cr content. For example, the resistivity of the S1 sample

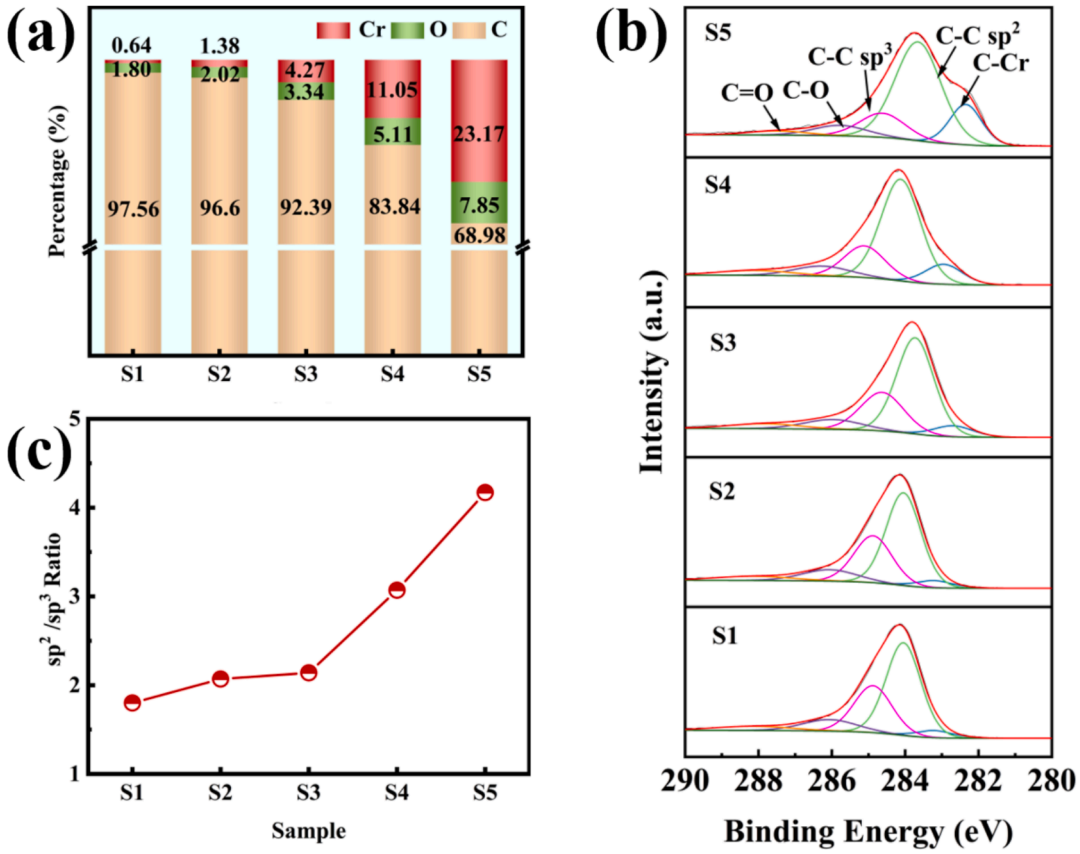

Fig. 3. XPS spectra of (a) content of Cr, O and C elements, (b) C 1 s spectra, (c) sp^2 content of Cr-DLC films.

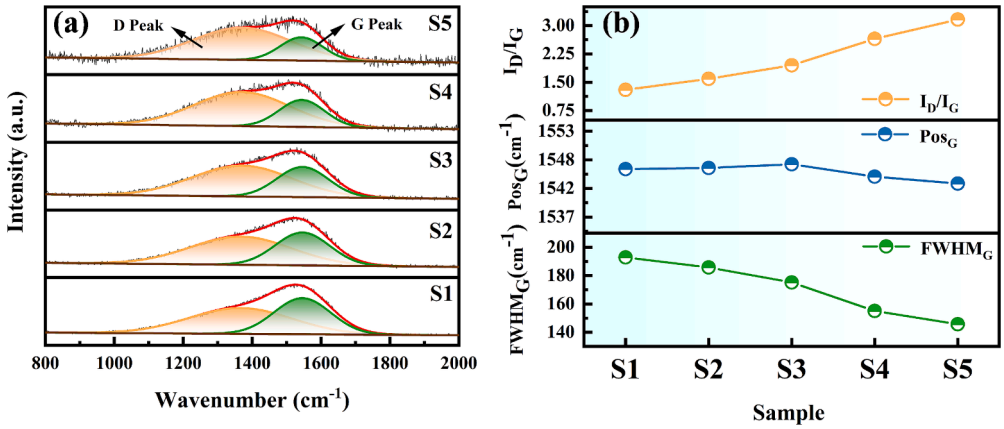

Fig. 4. (a) Raman spectra, (b) I_D/I_G, Pos_G and $FWHM_G$ of Cr-DLC films.

decreased from 1.8×10^6 Ω·mm at 150 K to 9.27×10^4 Ω·mm at 350 K, showing a decrease of 94.8 %. Similarly, the resistivity of the S5 sample decreased by 89.9 %. The TCR values were determined from the R-T plots using the following formula [45].

$$TCR = \frac{\rho_1 - \rho_0}{\rho_0} \times \frac{1}{T_1 - T_0} \times 10^6 \quad (2)$$

where ρ_1 and ρ_0 are the resistances of the sample at $T_1 = 350$ K and $T_0 = 100$ K, respectively. For all samples, the TCR values were negative, and their corresponding absolute values decreased monotonically from 4743 ppm/K to 4498 ppm/K as the Cr content increased from 0.64 at.% to 23.17 at.%, as shown in Fig. 7(b).

The carrier transport mechanism in Cr-DLC films can be analyzed by fitting the R-T curve, which relates the resistivity R of the amorphous semiconductor to the temperature T. The resistivity R and temperature T should satisfy the following formula [46–48].

$$R = R_0 \exp\left(\frac{T_0}{T}\right)^n \quad (3)$$

where R_0 and T_0 are constants. T_0 is the characteristic temperature associated with the activation energy, and R_0 is pre-exponential index. The value of n represents different electron transport mechanisms and the hopping dimensionality. Specifically, $n = 1$ means that the electron transport mechanism belongs to thermal activation, $n = 1/2$ corresponds to Efors-Shklovskii (ES) type two-dimensional variable range hopping (VRH), and n = 1/4 corresponds to Mott-type three-dimensional VRH.

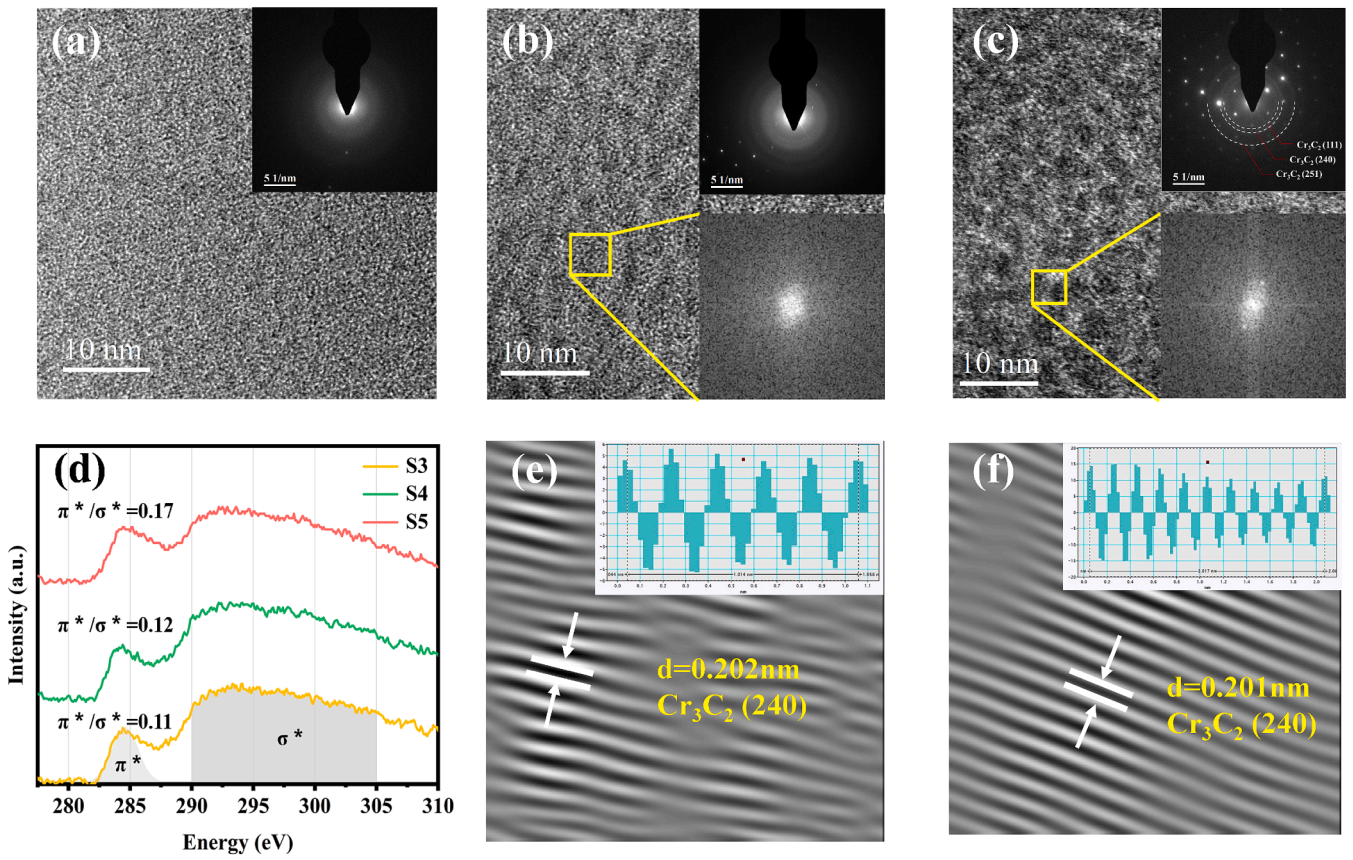

Fig. 5. HRTEM images and SAED of Cr-DLC films with (a) 4.27 at.%, (b)11.05 at.%, (c) 23.17 at.% Cr content, (d) corresponding EELS result, and inverse Fourier transform images of Cr-DLC with (e) 11.05 at.% and (f) 23.17 at.% Cr content.

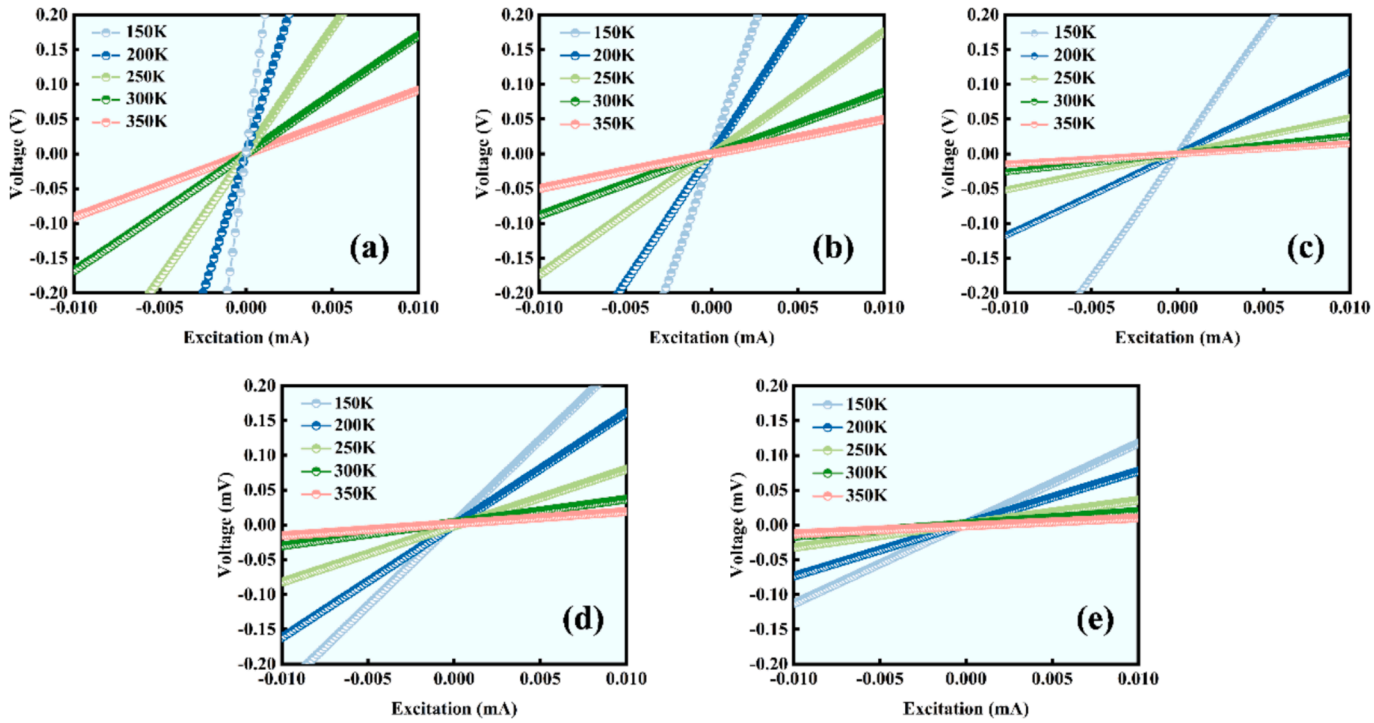

Fig. 6. I-V curves of the Cr-DLC films with (a) 0.64 at.%, (b) 1.38 at.%, (c) 4.27 at.%, (d) 11.05 at.%, and (e) 23.17 at.% Cr content from 150 K-350 K.

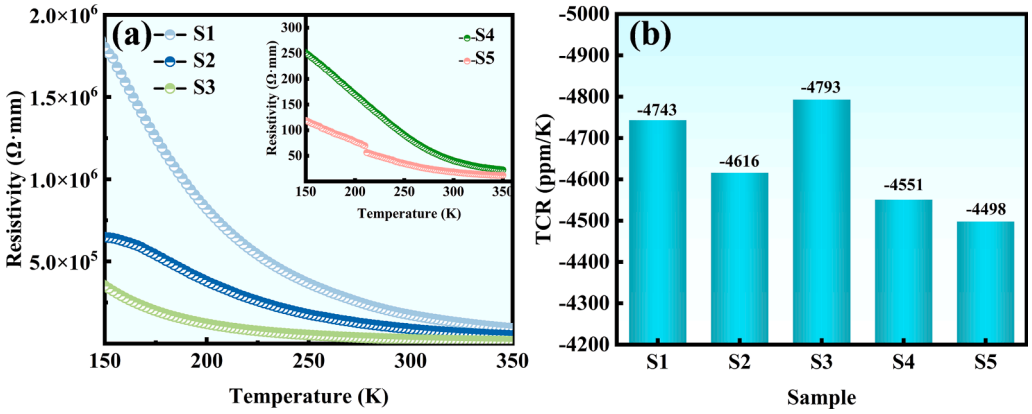

Fig. 7. (a) R-T behaviors and (b) TCR of samples S1-S5.

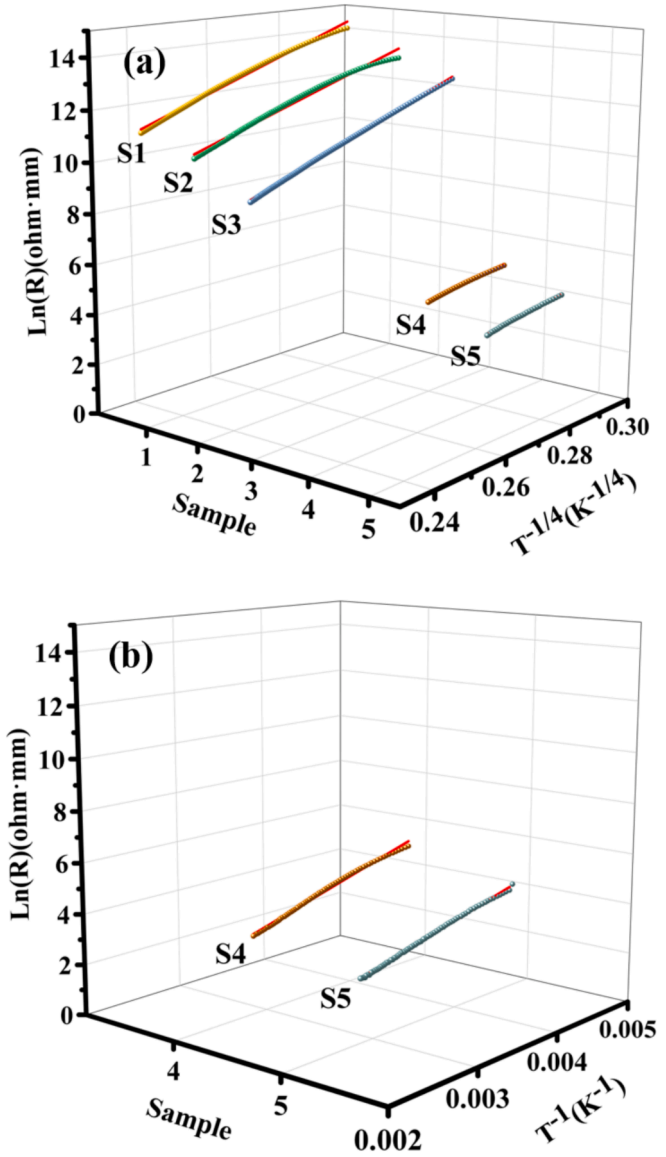

Fig. 8. Relationship between (a) Ln(R)- $T^{-1/4}$ under temperature ranges from 150 K to 350 K for S1-S3 and 210 K to 350 K for S4, S5, (b) Ln(R)- T^{-1} under temperature ranges from 150 K to 210 K. The red lines are fitting results.

Fig. 8 presents the fitting results of Cr-DLC with test temperatures range from 150 K to 350 K. For the S1, S2, and S3 samples with lower Cr content, Ln(R) exhibited a linear relationship with $T^{-1/4}$ within the temperature range of 150 K-350 K, suggesting that three-dimensional VRH conduction was the primary transport mechanism, as shown in Fig. 8(a). As for the S4 and S5 samples with higher Cr content, two predominant transport mechanisms over the entire temperature interval. As shown in Fig. 8(a) and (b), the Ln(R) and $T^{-1/4}$ of S4 and S5 samples had a linear relationship within 150 K-210 K, indicating the three-dimensional VRH conduction. In the higher temperatures interval 210 K-350 K, Ln(R) exhibited a linear relationship with T^{-1}, suggesting the thermal activation characteristic.

The local electrical properties of Cr-DLC films with Cr concentrations of 4.27 at.%, 11.05 at.%, and 23.17 at.% were investigated by C-AFM. In Fig. 9(a-c), the brightness of the regions in the images can reflect the variation in their electrical conductivity, where brighter regions indicated higher electrical conductivity. From a morphological point of view, at a low Cr content of 4.27 at.%, the conductive phases in the bright zones appeared small dots. With the increment of Cr content, the proportion of conductive phases raised and their size enlarged at a Cr content of 23.17 at.%, some of the conductive phases interconnected with each other. In addition, the I-V curves of the bright spots were obtained by ramping the bias voltage from −1 to + 1 V. The I-V curves of all samples showed good symmetry, and a limiting voltage (V_{max}) was observed for each sample. When the applied voltage was greater than V_{max}, the current exceeded the upper test limit of the equipment. As the Cr content increased from 4.27 at.% to11.05 at.% and then to 23.17 at.%, V_{max} decreased in an orderly manner from 0.39 V, 0.29 V to 0.20 V. In Fig. 9(d), at a low Cr content of 4.27 at.%, a threshold voltage (V_{thr}) was observed, and the current was barely detectable in the sample when the applied voltage was below V_{thr}. When the applied voltage surpassed V_{thr}, the current raised significantly. In contrast, Fig. 9(e) and 9(f) shows when the Cr content exceeded 11.05 at.%, V_{thr} disappeared, indicating a change in the carrier transport mechanism.

3.3. Energy band structure

The optical bandgap of the amorphous carbon material can be obtained using the Tauc plot method, which involves plotting the absorption coefficient (α) against the photon energy ($h\nu$) by the following equation [49]:

$$(\alpha h\nu) = A\left(h\nu - E_g\right)^n \tag{4}$$

where A is a constant and Eg represents the optical bandgap. The exponent n depends on the semiconductor material and the type of transition, and it can take values of 1/2, 3/2, 2, and 3. For direct bandgap semiconductors, such as DLC [50] the value of n is typically

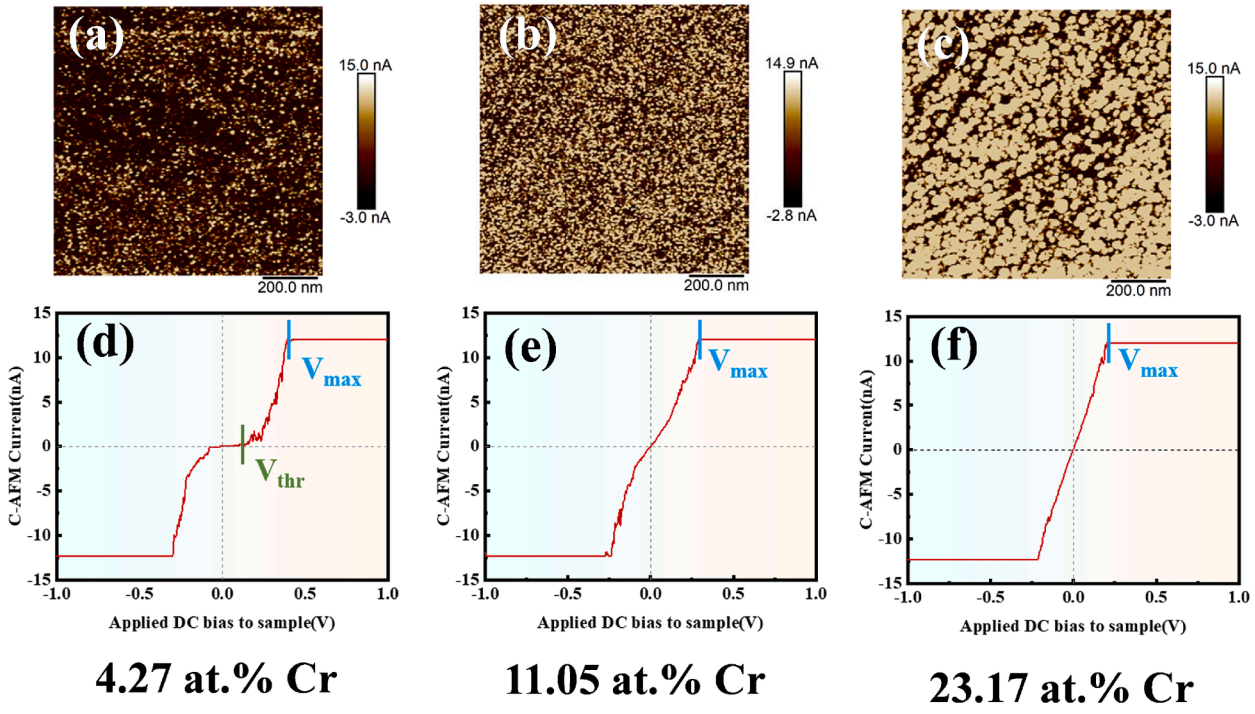

Fig. 9. The C-AFM images and corresponding I-V plots for the sample with 4.27 at.% Cr atoms (a), (d); 11.05 at.% Cr atoms (b), (e) and 23.17 at.% Cr atoms (c), (f).

taken as 1/2. The absorption coefficient α is defined as the fractional decrease in incident light intensity per unit increase in distance. The value of α can be calculated using Beer-Lambert's law equation [51].

$$\alpha = \frac{1}{d}\left[ln\left(\frac{1}{T}\right)\right] \quad (5)$$

where d is the thickness of the film and T is the measured transmittance.

Electrical tests in Fig. 7 confirmed that the Cr-DLC films exhibited typical semiconductor properties, and the samples can be considered as semiconductors. Fig. 10(a) illustrates that the transmittance of the S1-S5 samples decreased with increasing Cr content. Their $(\alpha h\nu)^2$ versus $h\nu$ curves are shown in Fig. 10(b). With the increase of Cr content, the optical bandgap Eg of S1-S5 samples decreased from 3.55 eV at 0.64 at.% Cr content to 2.49 eV at 23.17 at.% (Fig. 10(c)), which may be related to the change of the sp^2-C/sp^3-C ratio [52,53].

According to the band theory, the carrier transport is related to the work function (W_F) of the sample, which can be measured using ultraviolet photoelectron spectroscopy (UPS) [54]. As illustrated in Fig. 11(a) and (b), by identifying the secondary electron cut-off (E_{cut}) energy and the position of the Fermi level, the W_F can be obtained using the following equation [55].

$$W_F = h\nu - (E_{cut} - E_F) \quad (6)$$

where $h\nu$ is the energy of the photons (21.22 eV) emitted by the Helium (He) I discharge lamp, E_{cut} is the secondary electron cutoff energy, and E_F is the Fermi level. The UPS test directly takes the E_F as the energy reference point, and no bias voltage was applied to the sample during the test. Therefore, the binding energy $E_B = 0$ corresponds to the E_F. The W_F of Cr-DLC was calculated to be in the range of 4.26 eV to 4.39 eV, indicating that the doping of Cr had a slight effect on the W_F of the Cr-DLC film. Fig. 11(b) shows the valence band offsets (E_F-E_V, where E_F is the Fermi level and E_V is the valence band edge) for the S1-S5 samples [56]. The valence band offsets exhibited a tendency to decrease and then increase with the increase in Cr content. Combined with the measured optical bandgap, the band alignment of the S1-S5 samples is shown in Fig. 11(c) with vacuum energy level (0 eV) as a reference. The E_F of the S1-S5 samples were closer to the E_V, indicating that the Cr-DLC films in this study were p-type semiconductors, with holes as majority carriers.

3.4. Piezoresistive properties and related mechanisms

As shown in Fig. 12. the GF of the S2 sample was the highest, with a value of 22.8. However, as the increase of Cr content in the Cr-DLC film

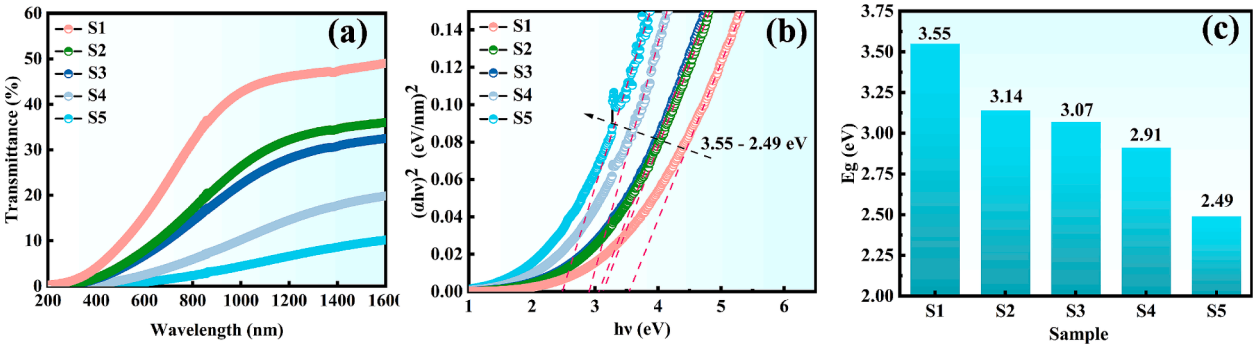

Fig. 10. Cr-DLC films with different Cr content (a) transmittance curves, (b) $(\alpha h\nu)^2$-hν curves and (c) optical bandgap.

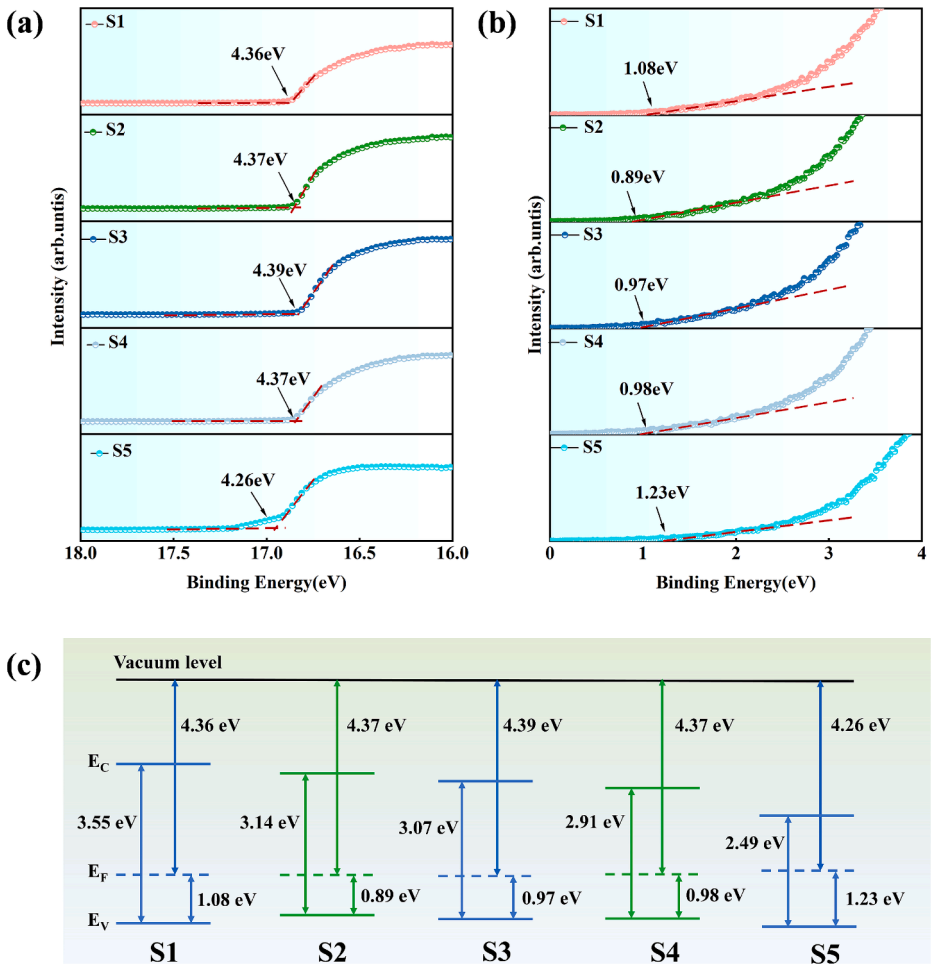

Fig. 11. (a) Secondary electron cut-off energy, (b) Fermi level positions, and (c) band alignment for the samples S1-S5.

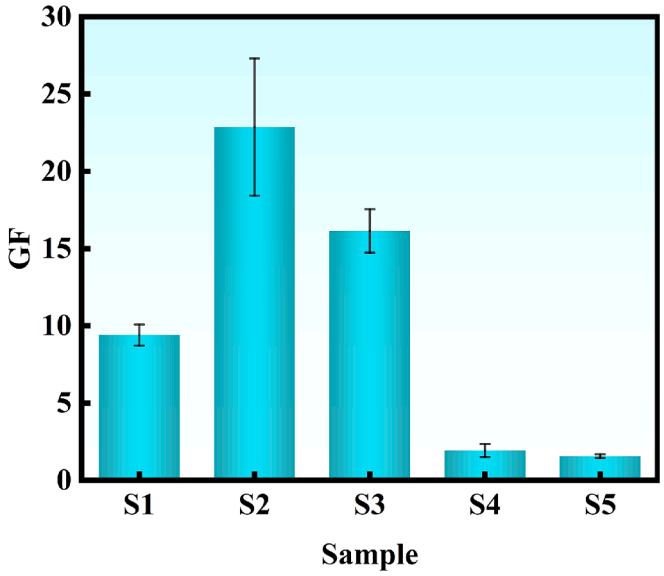

Fig. 12. GF testing results for samples S1-S5.

increased, the GF decreased rapidly, reaching a value of 1.6 for the S5 sample.

According to HRTEM analysis, when the Cr content was low, the doped Cr atoms were dissolved within the DLC matrix. However, under higher Cr content, Cr_3C_2 nanocrystals were formed [57]. Therefore, Cr-DLC films can be considered as a composite consisting of conductive sp^2 clusters, dissolved Cr atoms or Cr_3C_2 nanocrystals embedded within an insulating sp^3 matrix. Consequently, the carrier tunneling mechanism in Cr-DLC films can be described by the percolation-tunneling theory [21]. The conductivity of these films and the volume fraction of the conductive phase satisfy the following relationship [58,59].

$$\sigma \propto (x - x_c)^t \tag{7}$$

where σ is the conductivity, x is the volume fraction of the conductive phase, x_c is the threshold, and t is the transport index.

Combined with the I-V curves obtained from the C-AFM test in Fig. 9, it was observed that the V_{thr} existed at low Cr content. This indicated that carriers were transported between isolated conductive phases by tunneling, in this case of $x < x_c$. However, when the Cr content reached 11.05 at.%, the interconnection between the conductive phases led to the disappearance of the V_{thr}. In this case, percolation held a dominant position in carrier transport, despite the fact that $x < x_c$. Based on these observations, a simple carrier transport model was proposed to explain the electrical properties and piezoresistive effects of Cr-DLC films, as illustrated in Fig. 13. In this model, the sp^2 phase and the Cr/Cr_3C_2 conductive phase were distributed within the sp^3 insulating matrix.

In this particular scenario, the tunneling theory and the thick-film resistors (TFRs) model can be employed to analyze their piezoresistive behavior, and the GF can be characterized by the following equation [60]:

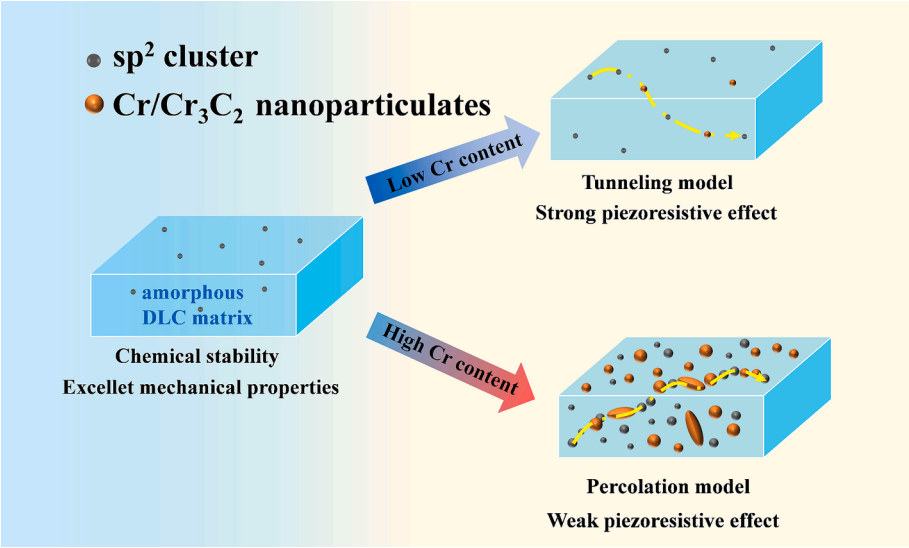

Fig. 13. Schematic diagram of the carrier transport mechanism of Cr-DLC films.

$$GF = \frac{\Delta R}{R \bullet \varepsilon} \simeq \frac{2d}{\xi} \quad (8)$$

where d is the average distance between neighboring conductive phases and ξ is the localization length.

According to Raman and TEM analysis, when the Cr content was low, the size of conductive sp^2 clusters and dissolved Cr atoms was smaller, resulting in a larger average distance between the conductive phases. Combined with the above-mentioned C-AFM in Fig. 9, carriers were conducted between isolated conductive phases through tunneling. Therefore, under a certain applied strain, the tunneling process can be significantly influenced by the average distance, leading to a notable change in resistivity–that is, a more pronounced piezoresistive effect. Similarly, as the Cr content increased, more conductive sp^2 and Cr_3C_2 phases were distributed within the sp^3 insulating matrix. The reduction in distance d resulted in the disappearance of the V_{thr}, and their carrier transport was dominated by percolation, showing a lower GF value. Furthermore, with an appropriate Cr content, the Fermi level E_F of sample S2 was much closer to E_V, indicating that the hole generation became easier with external energy input [61]. Under applied strain, the energy band structure of the semiconductor changed [62–64], which may affect both the carrier concentration and the tunnelling process between the conductive phases, resulting in the largest change in resistance and demonstrating the most significant piezoresistive effect.

4. Conclusion

The doped Cr atoms exhibit catalytic effect on the generation of sp^2 bonds in DLC film. As Cr the content increased from 0.64 at.% to 23.17 at.%, both the content and size of the conductive phase in the Cr-DLC films increased. Notably, when the Cr content reached 11.05 at.%, Cr_3C_2 nanocrystals emerged within the sp^3 matrix. In the temperature range of 150 K-350 K, the resistivity of the films decreased with increasing temperature, displaying semiconductor characteristics. Specially, the samples with Cr contents of 0.64 at.%, 1.38 at.% and 4.27 at.% exhibited three-dimensional Mott-type VRH conduction over the entire temperature range. However, the samples with Cr contents of 11.05 at.% and 23.17 at.% exhibited three-dimensional Mott-type VRH conduction from 150 K to 210 K, and thermal activation conduction from 210 K to 350 K.

Furthermore, doping with Cr atoms modulated the bandgap of the DLC films, causing the optical bandgap to narrow with increasing of Cr content. With the Cr content of 1.38 at.%, the Fermi level of the Cr-DLC film was closest to the E_V, resulting in the highest GF of 22.8. By combining with C-AFM tests and the carrier tunneling process of the conductive phase within the sp^3 matrix, a straightforward carrier transport model was proposed to explain the piezoresistive effect and electrical behavior of Cr-DLC films.

CRediT authorship contribution statement

Wenlong Zhang: Writing – original draft, Visualization, Validation, Investigation, Formal analysis, Data curation, Conceptualization. **Peng Guo:** Writing – review & editing, Visualization, Project administration, Investigation, Funding acquisition, Conceptualization. **Yulong Yang:** Investigation, Data curation. **Hao Li:** Investigation, Data curation. **Wei Yang:** Investigation, Formal analysis, Data curation. **Rende Chen:** Methodology, Investigation. **Bo Xie:** Methodology, Investigation, Data curation. **Aiying Wang:** Writing – review & editing, Visualization, Resources, Project administration, Funding acquisition.

Declaration of competing interest

The authors declare that they have no known competing financial interests or personal relationships that could have appeared to influence the work reported in this paper.

Acknowledgment

This research was supported by the National Natural Science Foundation of China (U20A20296, 52127803) and the Science and Technology Innovation 2025 Major Project of Ningbo (2023Z021). The authors wish to thank the assistance of Lijing Miao and Kemin Jiang at public Technology center, Ningbo Institute of Materials Technology and Engineering, Chinese Academy of Sciences for XPS measurement and discussion.

Appendix A. Supplementary data

Supplementary data to this article can be found online at https://doi.org/10.1016/j.apsusc.2025.162663.

Data availability

Data will be made available on request.

References

[1] A.T. Tulaev, A.S. Kozlov, J.V. Belyaev, V.V. Loboda, M.A. Bellavin, A.S. Korotkov, MEMS pressure sensors design, simulation, manufacturing, interface circuits: a review, IEEE Sens. J. 24 (2024) 7395–7405.
[2] S. Raman, K. Meena, S. Vetrivel, A.R. Sankar, Silicon nanowire piezoresistor and its applications: a review, Nanotechnology 35 (2024) 362003.
[3] A.A. Barlian, W.T. Park, J.R. Mallon, A.J. Rastegar, B.L. Pruitt, Review: semiconductor piezoresistance for microsystems, Proc. IEEE 97 (2009) 513–552.
[4] A.S. Fiorillo, C.D. Critello, S.A. Pullano, Theory, technology and applications of piezoresistive sensors: a review, Sens. Actuator A-Phys. 281 (2018) 156–175.
[5] H.P. Phan, D.V. Dao, P. Tanner, J.S. Han, N.T. Nguyen, S. Dimitrijev, G. Walker, L. Wang, Y. Zhu, Thickness dependence of the piezoresistive effect in p-type single crystalline 3C-SiC nanothin films, J. Mater. Chem. C 2 (2014) 7176–7179.
[6] Y.Z. Zhu, K.L. Cooper, G.R. Pickrell, A. Wang, High-temperature fiber-tip pressure sensor, J. Lightwave Technol. 24 (2006) 861–869.
[7] J. Robertson, Diamond-like amorphous carbon, Mater. Sci. Eng. R-Rep. 37 (2002) 129–281.
[8] A. Catena, Q.C. Guo, M.R. Kunze, S. Agnello, F.M. Gelardi, S. Wehner, C.B. Fischer, Morphological and chemical evolution of gradually deposited diamond-like carbon films on polyethylene terephthalate: from subplantation processes to structural reorganization by intrinsic stress release phenomena, ACS Appl. Mater. Interfaces 8 (2016) 10636–10646.
[9] K.S. Li, G. Xu, X.B. Wen, J. Zhou, F. Gong, High-temperature friction behavior of amorphous carbon coating in glass molding process, Friction 9 (2021) 1648–1659.
[10] S. Bhowmick, S. Shirzadian, A.T. Alpas, High-temperature tribological behavior of Ti containing diamond-like carbon coatings with emphasis on running-in coefficient of friction, Surf. Coat. Technol. 431 (2022) 127995.
[11] H. Khanmohammadi, W. Wijanarko, S. Cruz, M. Evaristo, N. Espallargas, Triboelectrochemical friction control of W- and Ag-doped DLC coatings in water-glycol with ionic liquids as lubricant additives, RSC Adv. 12 (2022) 3573–3583.
[12] M. Petersen, R. Bandorf, G. Bräuer, C.P. Klages, Diamond-like carbon films as piezoresistors in highly sensitive force sensors, Diam. Relat. Mater. 26 (2012) 50–54.
[13] A. Tibrewala, E. Peiner, R. Bandorf, S. Biehl, H. Luthje, Longitudinal and transversal piezoresistive effect in hydrogenated amorphous carbon films, Thin Solid Films 515 (2007) 8028–8033.
[14] A. Tibrewala, E. Peiner, R. Bandorf, S. Biehl, H. Lüthje, Transport and optical properties of amorphous carbon and hydrogenated amorphous carbon films, Appl. Surf. Sci. 252 (2006) 5387–5390.
[15] S. Meskinis, R. Gudaitis, V. Kopustinskas, S. Tamulevicius, Electrical and piezoresistive properties of ion beam deposited DLC films, Appl. Surf. Sci. 254 (2008) 5252–5256.
[16] S. Meskinis, R. Gudaitis, K. Slapikas, A. Vasiliauskas, A. Ciegis, T. Tamulevicius, M. Andrulevicius, S. Tamulevicius, Giant negative piezoresistive effect in diamond-like carbon and diamond-like carbon-based nickel nanocomposite films deposited by reactive magnetron sputtering of Ni target, ACS Appl. Mater. Interfaces 10 (2018) 15778–15785.
[17] A. Tibrewala, E. Peiner, R. Bandorf, S. Biehl, H. Lüthje, The piezoresistive effect in diamond-like carbon films, J. Micromech. Microeng. 17 (2007) S77–S82.
[18] R. Gudaitis, S. Meskinis, K. Slapikas, M. Andrulevicius, G. Niaura, S. Tamulevicius, Piezoresistive and electrical properties of Cr containing diamond-like carbon films, Surf. Coat. Technol. 211 (2012) 80–83.
[19] M. Grein, R. Bandorf, K. Schiffinann, G. Bräuer, Material structure and piezoresistive properties of niobium containing diamond-like-carbon films, Surf. Coat. Technol. 357 (2019) 273–279.
[20] T. Takeno, H. Miki, T. Sugawara, Y. Hoshi, T. Takagi, A DLC/W-DLC multilayered structure for strain sensing applications, Diam. Relat. Mater. 17 (2008) 713–716.
[21] S. Meskinis, R. Gudaitis, A. Vasiliauskas, A. Ciegis, K. Slapikas, T. Tamulevicius, M. Andrulevicius, S. Tamulevicius, Piezoresistive properties of diamond like carbon films containing copper, Diam. Relat. Mater. 60 (2015) 20–25.
[22] C.L. Yan, P. Guo, J.Y. Zhou, R.D. Chen, A.Y. Wang, Dependence of piezoresistive behavior upon Cu content in Cu-DLC nanocomposite films, Diam. Relat. Mater. 136 (2023) 109935.
[23] E. Peiner, A. Tibrewala, R. Bandorf, S. Biehl, H. Lüthje, L. Doering, Micro force sensor with piezoresistive amorphous carbon strain gauge, Sens. Actuator A-Phys. 130 (2006) 75–82.
[24] R. Koppert, D. Goettel, O. Freitag-Weber, G. Schultes, Nickel containing diamond like carbon thin films, Solid State Sci. 11 (2009) 1797–1800.
[25] X.W. Li, K.R. Lee, A.Y. Wang, Chemical bond structure of metal-incorporated carbon system, J. Comput. Theor. Nanosci. 10 (2013) 1688–1692.
[26] X.W. Li, A.Y. Wang, K.R. Lee, First principles investigation of interaction between impurity atom (Si, Ge, Sn) and carbon atom in diamond-like carbon system, Thin Solid Films 520 (2012) 6064–6067.
[27] S. Tamulevicius, S. Meskinis, T. Tamulevicius, H.G. Rubahn, Diamond like carbon nanocomposites with embedded metallic nanoparticles, Rep. Prog. Phys. 81 (2018) 024501.
[28] M. Tomidokoro, S. Tunmee, U. Rittihong, C. Euaruksakul, R. Supruangnet, H. Nakajima, Y. Hirata, N. Ohtake, H. Akasaka, Electrical conduction properties of hydrogenated amorphous carbon films with different structures, Materials 14 (2021) 2355.
[29] X.W. Li, P.L. Ke, A.Y. Wang, Probing the stress reduction mechanism of diamond-like carbon films by incorporating Ti, Cr, or W carbide-forming metals: Ab initio molecular dynamics simulation, J. Phys. Chem. C 119 (2015) 6086–6093.
[30] W. Dai, P.L. Ke, A.Y. Wang, Microstructure and property evolution of Cr-DLC films with different Cr content deposited by a hybrid beam technique, Vacuum 85 (2011) 792–797.
[31] W. Dai, A.Y. Wang, Synthesis, characterization and properties of the DLC films with low Cr concentration doping by a hybrid linear ion beam system, Surf. Coat. Technol. 205 (2011) 2882–2886.
[32] S.Y. Li, H. Li, J. Wei, G.S. Ma, R.D. Chen, K. Nishimura, P. Guo, P.L. Ke, A.Y. Wang, Nodular defects aggravated tribocorrosion failure mechanism in Cr/GLC multilayer coatings for marine applications, J. Mater. Res. Technol-JMRT 30 (2024) 6470–6481.
[33] W. Dai, G.S. Wu, A.Y. Wang, Preparation, characterization and properties of Cr-incorporated DLC films on magnesium alloy, Diam. Relat. Mater. 19 (2010) 1307–1315.
[34] S.M. Bae, S. Horibata, Y. Miyauchi, J. Choi, Tribochemical investigation of Cr-doped diamond-like carbon with a MoDTC-containing engine oil under boundary lubricated condition, Tribol. Int. 188 (2023) 108849.
[35] X. Ma, X.S. Tong, P. Guo, Y.L. Zhao, Q. Zhang, H.C. Li, R.D. Chen, A.Y. Wang, MEMS piezo-resistive force sensor based on DC sputtering deposited amorphous carbon films, Sens. Actuator A-Phys. 303 (2020) 111700.
[36] S.Z. Liu, Z.H. Zhao, W.L. Zhang, R.D. Chen, J. Wei, P. Guo, A.Y. Wang, Micron-scale Al particulates to improve the piezoresistive performance of amorphous carbon films, Diam. Relat. Mater. 143 (2024) 110926.
[37] A.I. Kulak, A.V. Kondratyuk, T.I. Kulak, M.P. Samtsov, D. Meissner, Electrochemical pulsed deposition of diamond-like films by powerful coulostatic discharge in dimethylsulfoxide solution of lithium acetylide, Chem. Phys. Lett. 378 (2003) 95–100.
[38] P. Guo, X.W. Li, L.L. Sun, R.D. Chen, P.L. Ke, A.Y. Wang, Stress reduction mechanism of diamond-like carbon films incorporated with different Cu contents, Thin Solid Films 640 (2017) 45–51.
[39] M. Jelinek, J. Zemek, M. Vandrovcová, L. Bacáková, T. Kocourek, J. Remsa, P. Písarík, Bonding and bio-properties of hybrid laser/magnetron Cr-enriched DLC layers, Mater. Sci. Eng. C-Mater. Biol. Appl. 58 (2016) 1217–1224.
[40] K. Hou, P.Y. Yi, X.B. Li, L.F. Peng, X.N. Lai, The effect of Cr doped in amorphous carbon films on electrical conductivity: characterization and mechanism, Int. J. Hydrog. Energy 46 (2021) 30841–30852.
[41] N. Paik, Raman and XPS studies of DLC films prepared by a magnetron sputter-type negative ion source, Surf. Coat. Technol. 200 (2005) 2170–2174.
[42] H. Sakata, G. Dresselhaus, M.S. Dresselhaus, M. Endo, Effect of uniaxial stress on the Raman spectra of graphite fibers, J. Appl. Phys. 63 (1988) 2769–2772.
[43] A.Y. Wang, K.R. Lee, J.P. Ahn, J.H. Han, Structure and mechanical properties of W incorporated diamond-like carbon films prepared by a hybrid ion beam deposition technique, Carbon 44 (2006) 1826–1832.
[44] H. Li, P. Guo, D. Zhang, R.D. Chen, X. Zuo, P.L. Ke, H. Saito, A.Y. Wang, Influence of deposition temperature on the structure, optical and electrical properties of a-C films by DCMS, Appl. Surf. Sci. 503 (2020) 144310.
[45] M. Petersen, U. Heckmann, R. Bandorf, V. Gwozdz, S. Schnabel, G. Bräuer, C. P. Klages, Me-DLC films as material for highly sensitive temperature compensated strain gauges, Diam. Relat. Mater. 20 (2011) 814–818.
[46] C.H. Wan, X.Z. Zhang, J. Vanacken, X.L. Gao, X. Zhang, L.H. Wu, X.Y. Tan, H. Lin, V.V. Moshchalkov, J. Yuan, Electro- and magneto-transport properties of amorphous carbon films doped with iron, Diam. Relat. Mater. 20 (2011) 26–30.
[47] C. Godet, S. Kumar, V. Chu, Field-enhanced electrical transport mechanisms in amorphous carbon films, Philos. Mag. 83 (2003) 3351–3365.
[48] P. Achatz, O.A. Williams, P. Bruno, D.M. Gruen, J.A. Garrido, M. Stutzmann, Effect of nitrogen on the electronic properties of ultrananocrystalline diamond thin films grown on quartz and diamond substrates, Phys. Rev. B 74 (2006) 155429.
[49] S. Majeed, K. Siraj, S. Naseem, M.F. Khan, M. Irshad, H. Faiz, A. Mahmood, Structural and optical properties of gold-incorporated diamond-like carbon thin films deposited by RF magnetron sputtering, Mater. Res. Express 4 (2017) 076403.
[50] B. Pandey, J. Mukherjee, B. Das, A.K. Kar, Nickel concentration dependent structural and optical properties of electrodeposited diamond like carbon thin films, Eur. Phys. J.-Appl. Phys 66 (2014) 10302.
[51] B. Pandey, S. Hussain, Effect of nickel incorporation on the optical properties of diamond-like carbon (DLC) matrix, J. Phys. Chem. Solids 72 (2011) 1111–1116.
[52] A. Hu, I. Alkhesho, H. Zhou, W.W. Duley, Optical and microstructural properties of diamond-like carbon films grown by pulsed laser deposition, Diam. Relat. Mater. 16 (2007) 149–154.
[53] B. Zhou, Z.B. Liu, D.G. Piliptsou, S.W. Yu, Z.F. Wang, A.V. Rogachev, A. S. Rudenkov, A. Balmakou, Structure and optical properties of Cu-DLC composite films deposited by cathode arc with double-excitation source, Diam. Relat. Mater. 69 (2016) 191–197.
[54] J.M. Zheng, Z.Q. Ying, Z.H. Yang, Z.D. Lin, H. Wei, L. Chen, X. Yang, Y.H. Zeng, X. F. Li, J.C. Ye, Polycrystalline silicon tunnelling recombination layers for high-efficiency perovskite/tunnel oxide passivating contact tandem solar cells, Nat. Energy 8 (2023) 1250–1261.
[55] T. Kamioka, Y. Hayashi, Y. Isogai, K. Nakamura, Y. Ohshita, Analysis of interface workfunction and process-induced damage of reactive-plasma-deposited ITO/SiO_2/Si stack, AIP Adv. 7 (2017) 095212.
[56] J.C. Chiu, S.L. Li, M.X. Lee, C.C. Yen, T.L. Chen, C.H. Chou, C.W. Liu, Performance improvement by double-layer a-IGZO TFTs with a top barrier, IEEE J. Electron Devices Soc. 10 (2022) 45–50.
[57] Y. Cai, H.D. Liu, Y. Ma, Q. Wan, H. Chen, Y. Liu, Y.M. Chen, Q.S. Mei, B. Yang, Effect of ion source current on the microstructure and properties of Cr-DLC coatings prepared by ion beam-assisted arc ion plating, Nano 12 (2017) 1750053.
[58] C. Grimaldi, Theory of percolation and tunneling regimes in nanogranular metal films, Phys. Rev. B 89 (2014) 214201.

[59] D. Toker, D. Azulay, N. Shimoni, I. Balberg, O. Millo, Tunneling and percolation in metal-insulator composite materials, Phys. Rev. B 68 (2003) 041403.
[60] C. Grimaldi, P. Ryser, S. Strässler, Gauge factor enhancement driven by heterogeneity in thick-film resistors, J. Appl. Phys. 90 (2001) 322–327.
[61] P. Chen, T. Du, H. Jia, L. Zhou, Q. Yue, H. Wang, Y. Wang, A novel Bi_2WO_6/Si heterostructure photocatalyst with Fermi level shift in valence band realizes efficient reduction of CO_2 under visible light, Appl. Surf. Sci. 585 (2022) 152665.
[62] N. Katoch, A. Kumar, R. Sharma, P.K. Ahluwalia, J. Kumar, Strain tunable Schottky barriers and tunneling characteristics of borophene/MX_2 van der Waals heterostructures, Phys. E. 120 (2020) 113842.
[63] J. Bi, G. Wei, M. Shang, F. Gao, B. Tang, W. Yang, Piezoresistance in Si_3N_4 nanobelts: toward highly sensitive and reliable pressure sensors, J. Mater. Chem. C 2 (2014) 10062–10066.
[64] X. Cheng, L. Wang, F.M. Gao, W.Y. Yang, Z.T. Du, D. Chen, S.L. Chen, The N and P co-doping-induced giant negative piezoresistance behaviors of SiC nanowires, J. Mater. Chem. C 7 (2019) 3181–3189.